Computational Mechanics (2020) 65:839–852
https://doi.org/10.1007/s00466-019-01797-x

ORIGINAL PAPER

Effective floating volume: a highly parallelizable mesh-free approach for solving transient multiphysics problems in multi-scale geometries with non-linear material properties

Reza Bahadori[1] · Hector Gutierrez[1]

Received: 22 June 2019 / Accepted: 13 November 2019 / Published online: 21 November 2019

Abstract
A novel numerical method is proposed for the solution of transient multi-physics problems involving heat conduction, electrical current sharing and Joule heating. The innovation consists of a mesh-free Monte Carlo approach that eliminates or drastically reduces the particle scattering requirements typical of conventional Monte-Carlo methods. The proposed algorithm encapsulates a volume around each point that affects the solution at a given point in the domain; the volume includes other points that represent small perturbations along the path of energy transfer. The proposed method is highly parallelizable and amenable for GPU computing, and its computational performance was substantially increased by the elimination of scattered interpolation. The accuracy and simulation time of the proposed method are compared against a finite element solution and also against experimental results from existing literature. The proposed method provides accuracy comparable to that of finite element methods, achieving an order of magnitude reduction in simulation time.

Keywords Mesh-free methods · Multiphysics simulation · Multi-scale systems · Monte-Carlo · Parallel computing · Superconducting quench

1 Introduction

Multiphysics boundary and initial value problems involve the simultaneous solution of partial differential equations on the spatial and time domains. Such problems are solved in state-of-the-art software using conventional numerical methods such as the finite difference method (FDM), finite volume method (FVM) or finite element method (FEM). Implicit versions of these methods involve matrix inversions, where the size of the matrices grows with the number of elements being used. Multi-scale multiphysics problems, where elements of significantly different dimensions are adjacent (e.g., a coil element and its insulation) can quickly become intractable with existing software tools, given the large memory requirements and prohibitive simulation time associated with a sufficiently large mesh needed to represent such elements while achieving reasonable accuracy. The Monte Carlo Method (MCM) [1–10] has emerged as an effective approach to solve boundary and initial value problems in systems that can be prohibitive to simulate by the conventional methods mentioned above. MCM relies on random number generation to solve the multi-dimensional integration associated with the solution of boundary value problems and can be implemented as either an on-grid or gridless method [11–14]. In mesh-free MCM, all points in the solution domain are solved independently, eliminating the requirement of generating a mesh and inverting the correspondingly (large) matrix, enabling to focus the solution in specific regions of interest without having to mesh and solve the entire domain [15–19]. Since the time history of each point in the domain can be solved independently, MCM is well suited for implementation in highly parallel platforms such as GPU computers. Haji Sheikh et al. [20] introduced both grid-based and grid-free Monte-Carlo methods to solve heat conduction problems in homogeneous media. Their method calculates the temperature at any point in the domain by adding the contributions of all probable sources around the point (sink) where energy can be received from. A novel version proposed by the authors extends this approach to nonlinear heat conduction in multilayer composite media [21–23]. These methods require scattering random particles and performing scattered interpolation to identify the value associated with each carrier

✉ Reza Bahadori
rbahadori2013@my.fit.edu

[1] Florida Institute of Technology, Melbourne, FL 32901, USA

particle in the physical domain. Computation of scattered interpolation is a very time-consuming step. In this paper, a novel approach is presented to significantly reduce simulation time in MCM by eliminating scattered interpolation at every step-length or iteration. Furthermore, this study addresses heat transfer in the presence of a very thin layer in a composite structure. The proposed method was demonstrated in the transient simulation of conductive heat transfer in a multiscale composite material with nonlinear material properties.

Various Mesh-free methods have been used to solve initial and boundary value problems such as heat conduction. Smoothed Particle Hydrodynamic (SPH) is one of the most prominent approaches. SPH [24] was originally described in astrophysics to model the motion of stars. SPH has been used in fluid mechanics and other applied physics problems, from large deformations in explosion events to heat transfer. A key aspect in SPH is the definition of a kernel function to avoid singularities in discrete physical systems. In 1999, Cleary [25] provided the formulation of heat conduction using SPH. The Mesh Free Galerkin (MFG) method is another important approach introduced in the early 1990s. MFG updates the kernel particle interpolant by an advanced version of the moving least squares (MLS) method to solve differential equations. Shepards interpolant [26] is also a version of MFG. Several other mesh-free methods have been used to obtain the thermal solution in a heat conduction problem, such as Finite Point Method [27], Boundary Knot Method [28], Radial Point Interpolation Method [29], etc. The proposed EFV method has significant advantages relative to these methods in that it performs a nearest point interpolation in the geometry around the energy transfer path only once (before starting a time iteration) and uses it to eliminate/minimize the requirement of scattered interpolation, leading to a significant reduction in simulation time.

In this paper, the derivation of the governing equations is shown in Sect. 2. The steady-state solution of the center point temperature in a sphere is combined with the transient Monte-Carlo solution. A modification is proposed to take thin layers into account. The governing equations for electric current sharing are obtained from combination of the steady-state solutions at the center point in a sphere and the steady-state Monte-Carlo solution. Next, the Joule heating equations are presented. Finally, the EFV algorithm is explained. Section 3 describes an example (quench in a superconducting tape) that considers the physics described above. The EFV method is verified numerically and experimentally in two different scenarios. Section 4 shows performance of the EFV method against FEM in terms of simulation time; and Sect. 5 provides conclusions.

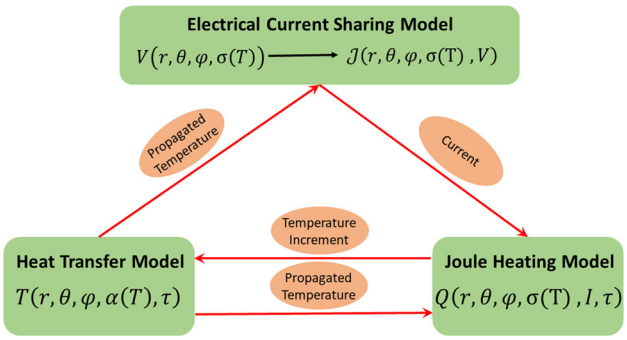

Fig. 1 Coupling of numerical models in the proposed multiphysics problem

2 Formulation and method

The multiphysics problem used to illustrate the proposed approach consists of the simulation of simultaneous heat conduction, electrical current sharing, and Joule heating. The governing equations and related modifications will be first presented to illustrate how the method can be extended to other multiphysics problems. Figure 1 shows the coupling scheme of the numerical models contributing to the proposed multiphysics problem, where T stands for temperature which is both spatial and time dependent. Time is shown as τ and r, θ and ϕ represent spherical coordinates: radius, elevation angle and azimuth angle, respectively. V is voltage, $\mathcal{J}$ is electric current density and Q is heat generated by Joule heating. α and σ are temperature dependent thermal diffusivity and electrical conductivity, respectively.

2.1 Heat transfer

A mesh-free method to solve transient heat conduction in composite structures has been shown in [22] and [23]. First, the steady-state solution of the temperature at the center of a sphere is derived, in a domain with space and temperature dependent thermal properties. To address time dependency, the distribution functions of transient floating random walk Monte-Carlo method in homogenous domains are used in combination with the steady-state solution. This also enables the evaluation of material properties in composite domains, as required to perform numerical integration. In this section, the proposed methods, their shortcomings and proposed solutions are discussed.

2.1.1 Steady-state conduction

The equation for the steady-state heat diffusion in spherical coordinates is:

$$\frac{1}{r^2 sin^2(\theta)}\frac{\partial}{\partial\varphi}\left(k(r,\theta,\varphi)\frac{\partial T(r,\theta,\varphi)}{\partial\varphi}\right) + \frac{1}{r^2 sin(\theta)}\frac{\partial}{\partial\theta}\left(k(r,\theta,\varphi)\sin((\theta)\frac{\partial T(r,\theta,\varphi)}{\partial\varphi}\right) + \frac{1}{r^2}\frac{\partial}{\partial r}\left(k(r,\theta,\varphi)r^2\frac{\partial T(r,\theta,\varphi)}{\partial r}\right) = 0 \quad (1)$$

Starting from (1), one can reach its integral form [Eq. (2)] by integrating from 0 to 2π in the azimuthal direction, from 0 to π in the elevation direction and from 0 to r in the radial direction:

$$\int_0^{2\pi}\int_0^{\pi}\sin(\theta)r^2k(r,\theta,\varphi)\frac{\partial T(r,\theta,\varphi)}{\partial r}d\theta d\varphi = 0 \quad (2)$$

The temperature at the center of the sphere based on the temperature of the particles in its vicinity forming a spherical region is defined using the coordinate transformations (3)–(5):

$$\eta = \frac{\int_0^r \frac{dr'}{k(r',\theta,\varphi)r^2\sin(\theta)}}{\int_0^R \frac{dr'}{k(r',\theta,\varphi)r^2\sin(\theta)}} \quad (3)$$

$$f = \frac{\int_0^\theta \frac{d\theta'}{\int_0^R \frac{dr'}{k(r',\theta',\varphi)r^2\sin(\theta)}}}{\int_0^\pi \frac{d\theta'}{\int_0^R \frac{dr'}{k(r',\theta',\varphi)r^2\sin(\theta)}}} \quad (4)$$

$$g = \frac{\int_0^\varphi\int_0^\pi \frac{d\theta'd\varphi'}{\int_0^R \frac{dr'}{k(r',\theta',\varphi')r^2\sin(\theta)}}}{\int_0^{2\pi}\int_0^\pi \frac{d\theta'd\varphi'}{\int_0^R \frac{dr'}{k(r',\theta',\varphi')r^2\sin(\theta)}}} \quad (5)$$

Applying the coordinate transformations to Eq. (2) yields the transformed integral shown in Eq. (6). Integrating from 0 to 1 with respect to η, yields (7):

$$\int_0^1\int_0^1\frac{\partial T(\eta,f,g)}{\partial\eta}dfdg = 0 \quad (6)$$

$$\int_0^1\int_0^1(T_R - T_C)dfdg = 0 \quad (7)$$

The central temperature in the sphere (T_C) is shown in Eq. (8) based on $T(R,\theta,\varphi)$ (temperature of sources around the center), where the thermal conductivity K is replaced by the thermal diffusivity α; the detailed derivation is shown in [23]:

$$T_C = \frac{\int_0^{2\pi}\int_0^{\pi}\frac{\sin(\theta)r^2T(R,\theta,\varphi)}{\int_0^R\frac{dr'}{\alpha(r',\theta,\varphi)}}d\theta d\varphi}{\int_0^{2\pi}\int_0^{\pi}\frac{r^2\sin(\theta)}{\int_0^R\frac{dr'}{\alpha(r',\theta,\varphi)}}d\theta d\varphi} \quad (8)$$

2.1.2 Monte-Carlo transient conduction

The floating random walk Monte-Carlo solution of three-dimensional transient heat conduction in homogenous media has been presented by Haji Sheikh et al. in [20]. Potential theory is used to describe the energy flow between source and sink. Starting from the transient heat conduction equation in spherical coordinates (1), the Monte-Carlo solution for the temperature at the center of a sphere at (x, y, z) is shown in Eq. (9) [30]; Eqs. (10)–(12) are probability functions in azimuth (φ), elevation (θ) and radial direction (r), respectively. The parameter (τ) is the time step.

$$T(x,y,z,t) = \int_{F=0}^1\int_{G=0}^1\int_{\tau=0}^t T(r,\varphi,\theta,t-\tau)\,dFdGdH^{(3)} \quad (9)$$

$$F(\varphi) = \frac{\varphi}{2\pi} \quad (10)$$

$$G(\theta) = \frac{1}{2}(1-cos\theta) \quad (11)$$

$$H^{(3)}\left(\frac{\alpha\tau}{r^2}\right) = 1 + 2\sum_{k=1}^{\infty}(-1)^k\exp\left(\frac{-k^2\pi^2\alpha\tau}{r^2}\right) \quad (12)$$

Calculation of step-length, elevation and azimuth angles for probable sources around each point requires generating random numbers RN_1–RN_3 as arguments to the inverse functions of Eqs. (10)–(12), shown in Eqs. (13)–(16). The corresponding curve fit coefficients D_i, $(i = 1-4)$ are shown in Table 1 [23,30,31]. The outcomes of Eqs. (13)–(16) are fed to Eq. (8) to conduct numerical integration and calculate the transient heat conduction in a composite layered structure.

$$\varphi = 2\pi(RN_1) \quad (13)$$

$$\theta = \cos^{-1}[1 - 2(RN_2)] \quad (14)$$

$$\frac{\alpha\tau}{r^2} = D_1 + D_2(RN_3) + D_3(RN_3)^2 + D_4(RN_3)^3 \quad RN_3 < 0.6 \quad (15)$$

$$\frac{\alpha\tau}{r^2} = -0.10132\,ln[0.5(1 - RN_3)] \quad RN_3 \geq 0.6 \quad (16)$$

2.1.3 Limitations

In the method presented above, the boundary value problem is solved by peripheral integration of the temperature at the boundaries, while the material properties inside the sphere along the path of energy transfer from source to sink are taken into account. To obtain material properties inside the sphere,

Table 1 Coefficients of the inverse probability function (15)

RN_3	D_1	D_2	D_3	D_4
0.0–0.1	0.079578	0.079621	0.058919	0.048997
0.1–0.3	0.079515	0.081077	0.048261	0.074542
0.3–0.6	0.070722	0.150740	−0.13699	0.240830

the algorithm divides the step-lengths r in an equal number of steps, then considers the thermal diffusivity at these points in the integration of Eq. (8). Figure 2a illustrates this approach in a cross section of a composite material where each layer has been defined by K points using a Halton set sequence. In this figure, only one particle (source of energy) is shown, but bear in mind that several particles are scattered around point K as defined by Eqs. (13)–(16) to find the uniform distribution of probable sources around the sink. Particle J depicts the jth probable source for point $k \in K$. The step-length r is divided into $M = 5$ sub step-lengths, dr. Before performing the peripheral integration (8), the location of particle J and points in between point K and particle J should be calculated, since they do not coincide with the location of points in K. Then, the temperature of particle J and the thermal diffusivity of points between α_2 and α_5 should be calculated. Since $k \in K$, α_1 is known from the initial condition or the previous time step. Scattered interpolation is the usual method to obtain these values—this is a significantly time consuming step. Figure 2b illustrates a shortcoming on this approach when simulating a multi-scale geometry. A very thin layer of material 2 is sandwiched between materials 1 and 3. The substantial difference in thickness defines a multi-scale geometry problem. In Figure 2b, none of the acquisition points between point k and particle J may fall in the narrow layer, and therefore material properties of this layer are not taken into account for the calculation of the center point temperature. A simple solution to address this issue is to increase the number of divisions such that size of each sub step-length is smaller than the size of the thin layer—this, however, leads to a very large number of sub step-lengths and therefore a prohibitive increase in simulation time. Furthermore, in some problems the initial condition is not homogenous in all layers, or heat generation may occur in the middle thin layer. In these cases, using only particle $J's$ temperature in the calculation of heat propagation is not sufficient: one should acquire the temperature of all points in between sink and source in addition to their material properties and consider all in the central temperature calculation.

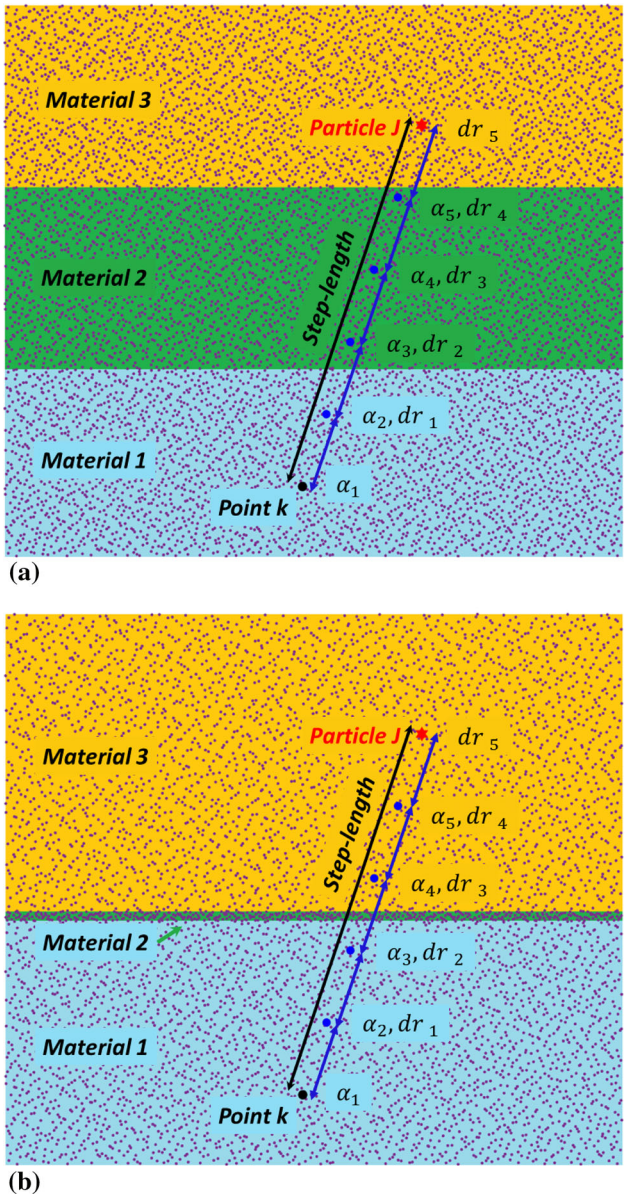

Fig. 2 A thin layer in a multi-scale domain using the division algorithm

2.1.4 Proposed approach: the effective floating volume

The issues mentioned above require modifications of the original method that can address these shortcomings. The proposed approach is called *effective floating volume* (EFV)—it meets accuracy requirements while providing significantly smaller simulation time. In the transient solution, step-length is calculated using Eqs. (15)–(16). A random number $0 \leq RN_3 \leq 1$ is generated, and $C(RN_3)$ is obtained by replacing RN_3 in Eqs. (15)–(16). The step-length r is then calculated as:

$$\frac{\alpha\tau}{r^2} = C(RN_3) \implies r = \left(\frac{\alpha\tau}{C(RN_3)}\right)^{1/2} \tag{17}$$

where $C(RN_3)$ is constant for each individual r. If the time step τ is constant during simulation, the magnitude of r for

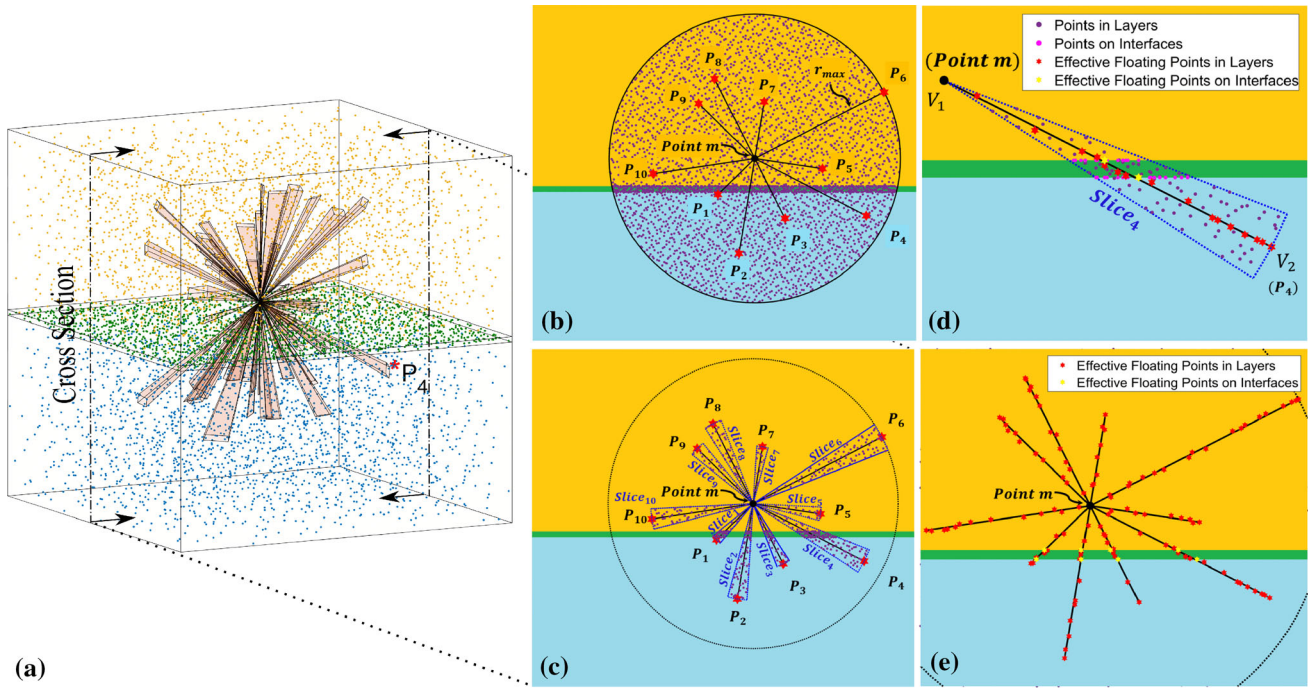

Fig. 3 Extracting an effective floating volume around point m using other points that define the geometry. (Color figure online)

each particle (probable source) depends only on the thermal diffusivity α. In nonlinear materials, thermal diffusivity can be a temperature dependent parameter. In that case, the maximum step-length for each point is found using Eq. (18), where α_{max} is the maximum value of thermal diffusivity in the temperature range, and $C(RN_3)_{min}$ is the minimum value of the right-hand side of Eqs. (15)–(16):

$$R_{max} = \left(\frac{\alpha_{max}\tau}{C(RN_3)_{min}} \right)^{1/2} \tag{18}$$

Figure 3a shows the three-dimensional representation of an "effective floating volume" around one point out of K points that define the geometry. Consider point $m \in K$: ten probable sources around m are displayed in the cross section of composite media shown in Fig. 3b. Out of K points representing the geometry, the points encapsulated in the sphere with radius R_{max} are chosen for further steps. This is the maximum number of points that may participate in the solution at point m. Changing temperature can only reduce the radius of this sphere, since it is directly related to the temperature-dependent thermal diffusivity, and its maximum value is already taken into account in the calculation of R_{max}. Each probable source is shown as $P_j \mid 1 < j < J, J = 10$. Figure 3c illustrates the next step, in which points surrounding the energy transfer path from each probable source to sink m are separated and labeled $Slice_j \mid 1 < j < J$. The volume around point m formed by points in the slices is used to perform the closest distance calculation. Each slice is a three-dimensional pyramidal volume, and only its cross section is shown here for the sake of clarity; some points have been added on the boundaries and interfaces between layers. Alternatively, the boundary and interface points for each layer can be extracted using the convex hull algorithm. Then, the points participating in the solution at point m are chosen among points in the slices. Figure 3d illustrates this step for $Slice_4$. The line between point m and P_4 is defined by V_1 and V_2; the distance of each point in $Slice_4$ to the line V_1V_2 is:

$$D_i = \|(\mathcal{P}_i - V_2) \times (V_1 - V_2)\| / \|V_1 - V_2\| \tag{19}$$

where $\mathcal{P}_i$ is the coordinate of the ith point in $Slice_4$ and D_i is the shortest distance to the line. This process is repeated for all slices around point m. The steps described in Fig. 3b, c reduce the computational load of Eq. (19) by avoiding performing the calculation for all K points, significantly reducing simulation time. Equation (19) is evaluated at points in both the material layers and the interfaces between layers, which ensures the correct definition of boundaries and interfaces when computing the solution at point m; effective floating points in layers are shown with red star markers and on interfaces with yellow star markers. Figure 3e shows the "effective floating volume" for point m formed by the points around it. The assumption is that all acquisition points share the energy transfer path from associated source to sink. To meet this assumption, the acquisition points must be able to slightly move. These points also participate in the solution of other

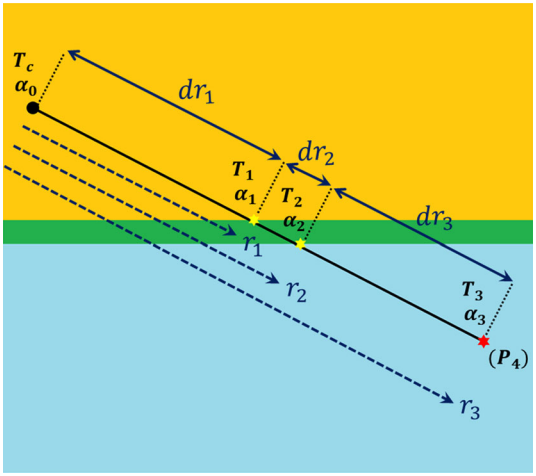

Fig. 4 Contributing variables in Eq. (22) in case of a thin layer

points in the geometry, and may be required to move in other directions to coincide with the path of energy transfer for those points. *The word "Floating" is used to represent the ability of points in the domain to meet this assumption*. Similar to other numerical methods (such as finite elements or finite differences) in which model accuracy is directly related to the number of elements, point density affects the accuracy of the proposed method, with error converging to zero as the number of points (elements) becomes increasingly larger. *All steps needed to find an effective floating volume around each point are performed only once,* before starting computing the solution in successive time iterations. At each time step, the steplengths of probable sources around each point will either be equal to their maximum values or will be smaller. In the first case, all effective floating points participate in the solution; in the second case, only the acquisition points whose radii are smaller than the corresponding steplength participate. If the number of acquisition points (M) is large enough to neglect the distance from a probable source (at the tip of the steplength) to the closest acquisition point in the respective direction, the interpolation process can be eliminated while keeping an acceptable bound in error. Otherwise, it is only required to do interpolation for the temperature and material properties of a probable source at the tip of the steplength, since the temperature and material properties of all other acquisition points in between are known either from the initial condition or from a previous time step in the solution. This reduces the use of scattered interpolation by a factor of $1/M$.

Equation (8) takes into account the temperature at the boundary and the material properties of all acquisition points inside the sphere. To include nonhomogeneous initial conditions, heat generation in a thin layer, etc. in the solution of a central temperature, the temperature of all acquisition points needs to participate in the solution equation. To clarify this, consider the energy transfer path from P_4 to point m in Fig. 3d, simplified to three acquisition points as shown in Fig. 4. Starting from the steadystate Eq. (6), the integration is split in three defined integrals from zero to 1, yielding the result on Eq. (20), where the expression inside the integral calculates the contribution of source P_4 on the central temperature T_C, where $dT_m = T_m - T_{m-1}$, and $m = 2, 3, \ldots, M$:

$$T_C = \int_0^1 \int_0^1 (T_1 + dT_2 + dT_3)\, df dg \tag{20}$$

Using Eqs. (4) and (5), $df dg$ is equal to:

$$df dg = \frac{\frac{d\theta d\varphi}{\int_0^R \frac{dr'}{K(r',\theta,\varphi)r^2\sin(\theta)}}}{\int_0^{2\pi}\int_0^{\pi} \frac{d\theta' d\varphi'}{\int_0^R \frac{dr'}{K(r',\theta',\varphi')r^2\sin(\theta)}}} \tag{21}$$

Substituting Eq. (21) in (20) leads to the general equation for the central temperature T_C :

$$T_C = \frac{\int_0^{2\pi}\int_0^{\pi} \frac{T_1(r,\theta,\varphi)+\sum_{m=2}^{M} dT_m(r,\theta,\varphi)}{\int_0^R \frac{dr'}{\sin(\theta)r^2\alpha(r',\theta,\varphi)}} d\theta d\varphi}{\int_0^{2\pi}\int_0^{\pi} \frac{1}{\int_0^R \frac{dr'}{r^2\sin(\theta)\alpha(r',\theta,\varphi)}} d\theta d\varphi} \tag{22}$$

Points, acquisition points, sinks, sources, and effective floating points are all the same points used to define the geometry of the problem at the beginning of the algorithm. The role these points take in the process of implementing the EFV algorithm is an important key to their names. The geometry (including layers and boundaries) is defined by a total number K uniformly distributed random points named by the sub-index k. Sinks and sources around point k are a subset of the points within the domain. Particles are a physical representation of energy transport between sources and sink. The number of particles is defined by the variable J, denoted individually by the sub-index j. Once the energy transfer paths are defined by particles connecting sources and sink, the EFV algorithm finds the $M \not\subset K$ number of closest points to each energy transfer path around the sink. These points are now called acquisition points for the energy transfer path j. The acquisition points are hence a subset of the total k points that define the geometry. The Effective Floating Volume for sink k consists of $J \times M$ acquisition points around sink k. One should be careful when defining the number of acquisition points M in the EFV method. The number of acquisition points should be larger than the maximum possible number of boundaries that may be crossed by the energy transfer path. This assures that layers are well defined in the EFV algorithm. Increasing the value of M beyond that means more points are inside the layers in the EFV. Since a nearest point algorithm is employed to define

the acquisition points, a large value to M causes far points in the energy transfer path to be attached to the EFV algorithm, which not only does not help accuracy but may increase error. M should be defined with respect to the point density of the geometry. We suggest to use the proportion of $6.LET/ADP$ to estimate the maximum number for M, where LET stands for Length of Energy Transfer" for the path between source and sink and ADP stands for Average Distance of Points" in the geometry. It is obtained by dividing volume of a cylinder along the energy transfer path with radius ADP by volume of each point as an sphere with radius $ADP/2$.

2.2 Electric current sharing

The current sharing model shown in Fig. 1 calculates the steadystate distribution of electric potential V at each time step, and uses it to calculate the electric current density $\mathcal{J}$. The assumption to model current sharing in heterogeneous material is that the effect of change in temperaturedependent electrical conductivity on the electric potential distribution can be modeled by a succession of steadystate propagation events. In heterogeneous media, Laplaces equation for the electric potential V can be written as:

$$\begin{aligned}&\frac{1}{r^2 sin^2(\theta)}\frac{\partial}{\partial\varphi}\left(\sigma(r,\theta,\varphi)\frac{\partial V(r,\theta,\varphi)}{\partial\varphi}\right)\\&+\frac{1}{r^2 sin(\theta)}\frac{\partial}{\partial\theta}\left(\sigma(r,\theta,\varphi)\sin(\theta)\frac{\partial V(r,\theta,\varphi)}{\partial\varphi}\right)\\&+\frac{1}{r^2}\frac{\partial}{\partial r}\left(\sigma(r,\theta,\varphi)r^2\frac{\partial V(r,\theta,\varphi)}{\partial r}\right)=0\end{aligned}\tag{23}$$

where σ is the electrical conductivity. This equation is similar to the steadystate heat conduction problem; hence, the methods described in Sects. 2.1.1–2 can be used. The steadystate electric potential at the center of the sphere is:

$$V_C=\frac{\int_0^{2\pi}\int_0^{\pi}\frac{\sin(\theta)r^2V(R,\theta,\varphi)}{\int_0^R\frac{dr'}{\sigma(r',\theta,\varphi)}}d\theta d\varphi}{\int_0^{2\pi}\int_0^{\pi}\frac{r^2\sin(\theta)}{\int_0^R\frac{dr'}{\sigma(r',\theta,\varphi)}}d\theta d\varphi}\tag{24}$$

The MonteCarlo solution is for the steadystate in this case. The MonteCarlo formulation for steadystate electric potential distribution in homogeneous media is similar to that for temperature in steadystate heat conduction [20]. Equations (25)–(27) define the steadystate electric potential at the center point of a sphere, and the corresponding probability functions in azimuth and elevation directions, respectively. Similarly, inverse probability functions (13)–(14) can be used to calculate the route of each probable source around the sink.

$$V(x,y,z)=\int_{F=0}^{1}\int_{G=0}^{1}\int_{\tau=0}^{t}V(r,\varphi,\theta)dFdG\tag{25}$$

$$F(\varphi)=\frac{\varphi}{2\pi}\tag{26}$$

$$G(\theta)=\frac{1}{2}(1-cos(\theta))\tag{27}$$

Since the steadystate problem is not dependent on time, the MonteCarlo approach suggests finding the furthest probable sources on the boundaries of the solution domain. Therefore, the solution for electrical potential at each point comes from the uniform distribution of sources around it that rest on the boundary. To account for temperature dependent electrical conductivity in multiscale composite media, the coordinate transformations (3)–(5) are applied to Eq. (23), where temperature and thermal diffusivity are replaced by electric potential and electrical conductivity. After coordinate transformation and splitting the integral in the radial direction, a relation for the steadystate electric potential V similar to Eq. (24) is found [Eq. (28)], with electrical resistivity σ where $dV_m=V_m-V_{m-1}$, and $m=2,3,\ldots,M$.

$$V_C=\frac{\int_0^{2\pi}\int_0^{\pi}\frac{V_1(r,\theta,\varphi)+\sum_{m=2}^{M}dV_m(r,\theta,\varphi)}{\int_0^R\frac{dr'}{r^2\sin(\theta)\sigma(r',\theta,\varphi)}}d\theta d\varphi}{\int_0^{2\pi}\int_0^{\pi}\frac{1}{\int_0^R\frac{dr'}{r^2\sin(\theta)\sigma(r',\theta,\varphi)}}d\theta d\varphi}\tag{28}$$

The acquisition points to solve numerically for electric potential lay on the longest possible transport path, i.e., from boundary to sink. If there are enough acquisition points to meet the accuracy requirements in each time step, they can be used for coupling the transient heat conduction and electrical current sharing problems. Finding the acquisition points need to be done only once the step shown in Fig. 2a is not needed, since acquisition points should touch the boundary. Once electric potential is found in the domain, the electric current density $\mathcal{J}$ is calculated by Eq. (29), where the sign indicates that the electric current points toward the decreasing direction of the electric potential gradient:

$$\mathcal{J}(r,\theta,\varphi)=-\sigma(r,\theta,\varphi)\nabla V(r,\theta,\varphi)+\frac{\partial D(r,\theta,\varphi)}{\partial\tau}\tag{29}$$

where D in Eq. (29) is current displacement or current flux density vector, defined as $D(r,\theta,\varphi)=\frac{\partial\varepsilon E(r,\theta,\varphi)}{\partial\tau}$ where ε is electrical permittivity and E is the electric field: $E(r,\theta,\varphi)=-\nabla V(r,\theta,\varphi)$.

2.3 Joule heating

Once current density is calculated, one can determine the electric current passing each point. The electrical resistance $\mathcal{R}$ of each point $k\in K$ can be calculated using the dimensions of each layer, the point density of that layer and the electrical

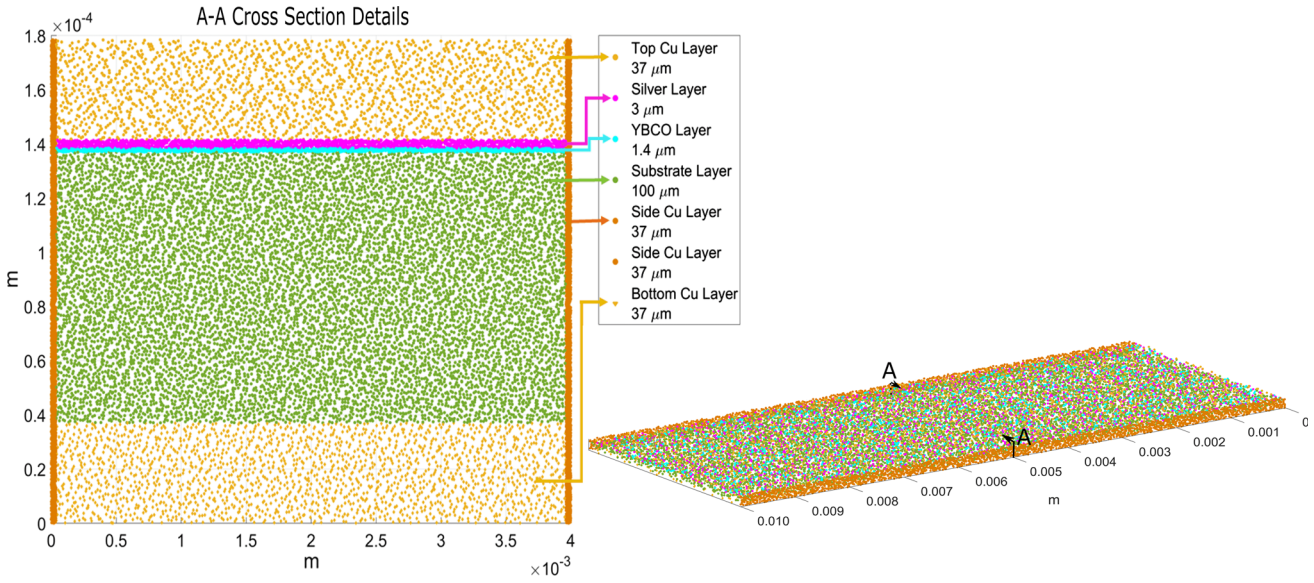

Fig. 5 YBCO tape and its cross-section, outlined by scattered random points

resistivity of each point at the respective temperature. Knowing the electrical current I and electrical resistance $\mathcal{R}$ at each point, the generated energy Q at each time step due to Joule heating (resistive dissipation) can be calculated as:

$$Q(r,\theta,\varphi) = \mathcal{R}(r,\theta,\varphi)I(r,\theta,\varphi)^2\tau \tag{30}$$

The temperature increment dT_k at each point $k \in K$ due to Joule heating can be obtained using Eq. (31), where C_p is the temperature dependent specific heat and m is the mass of each point in the domain:

$$dT_k = Q(r,\theta,\varphi)/m(r,\theta,\varphi)C_p(r,\theta,\varphi) \tag{31}$$

Since heat generation and heat propagation are happening at the same time, dT_k is added to all points before running the heat propagation algorithm [Eq. (22)], then the temperature of all points at the corresponding time step is stored.

3 Application example: current sharing during superconducting quench

Superconducting YBCO tapes (Yttrium Barium Copper Oxide) are good examples of composite materials with multi-scale geometry. The silver and YBCO layers in this sandwich structure have a thickness of approximately 3 μm and 1.4 μm, respectively. The YBCO layer is a superconducting material: it reaches near zero electrical resistance when persistent mode conditions are met, allowing the superconducting tape to carry a very large current with no Joule dissipation. The critical conditions to achieve superconductivity are a function of temperature, electric current density and magnetic field. The transition from superconducting state to normal conducting state is called quench. When quench happens, the electric resistivity of the YBCO layer increases drastically compared to other layers in the tape conductor. When the electric current passing through the near-zero resistance layer of YBCO reaches a quenched spot, it finds the lowest resistance path, forcing very large electrical currents through the stabilizer layers (copper and silver). Since the electrical resistivity of copper is not zero, Joule heating takes place. The heat generated in the copper layer propagates in both longitudinal and transverse directions simultaneously, raising the temperature in the YBCO layer above its critical temperature, causing expansion of the quench region in the direction of the heat transfer. Figure 5 shows the cross section geometry of a YBCO tape made of random points. The layer thicknesses have been scaled to illustrate the multi-scale geometry of this composite structure. The length of tape to be considered in this example is 0.01 m.

3.1 Effective floating volume (EFV): predictions compared to finite elements method

Superconducting quench can happen when the critical conditions for the superconducting material are exceeded (critical temperature, critical current density or critical magnetic field) or due to physical impurities in the tape, such as a crack that leads to a small area of high electrical resistance. To simulate a quench event, we assumed that a length of 1 mm at one end of the tape has a physical impurity. The electrical resistivity at this point in the YBCO layer is considered to be 500 μΩ m. Figure 6 shows the temperature dependent material properties used with both methods (EFV and FEM):

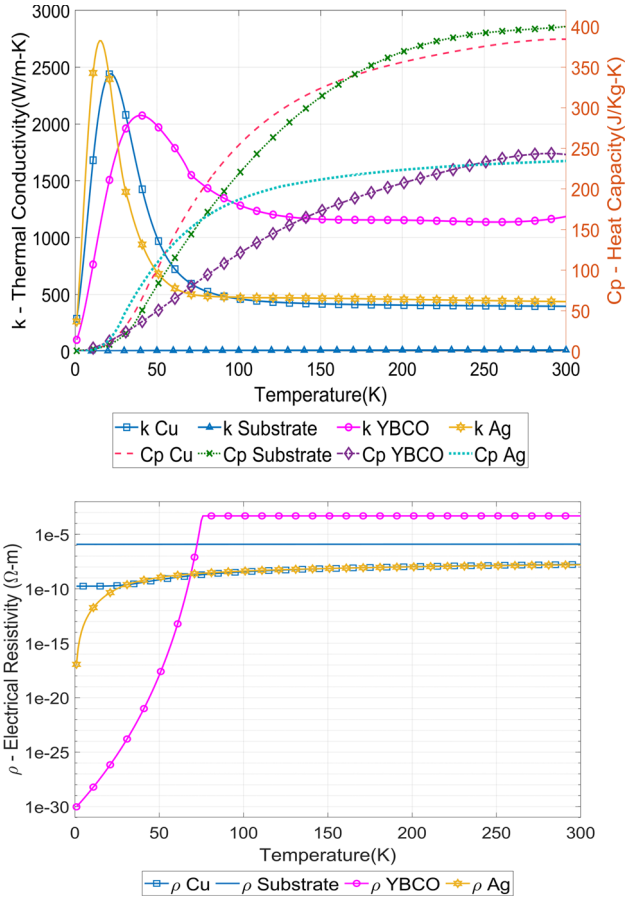

Fig. 6 Material properties in the YBCO tape as function of temperature

thermal conductivity, heat capacity and electrical resistivity of the different materials in the superconducting YBCO tape. Densities are considered constant (8940, 8890, 6390 and 10,490 kg/m^3 for copper, substrate, YBCO and Silver, respectively). A number of directions around the center points to look for probable sources of energy $J = 200$ was used in this example. The maximum number of acquisition points in the radial direction was set to $M = 15$. The superconducting tape has a terminal on one end with an electrical current $I = 300$ A, while the other end is connected to ground. The same geometry was implemented in a state-of-the-art finite element multiphysics solver (COMSOL), which will be used as benchmark of accuracy and performance of the proposed approach. The brick elements are swept along the length of the conductor. The number of random points for the EFV computation and the number of nodes in the FEM simulation was set to approximately 40,000, providing an equivalent baseline for comparison of accuracy and simulation time. The initial temperature was 40 K, which is below the critical temperature of YBCO (approximately 50 K). An electric current $I = 300$ A passes through the tape. The simulation is done with a time step of 3.3×10^{-4} s, reaching the final time $\tau = 0.1$ s in 300 time steps. Figure 7 shows the temperature rise on points distributed evenly (at 0.25 cm intervals) in the YBCO layer along the length of the tape versus time. The results from both methods lie within an error margin that confirms the accuracy of the proposed EFV method. Figure 8 shows the temperature distribution (top view) on the superconducting tape at three different times steps, ranging from the beginning of the simulation to 0.04 s. Current sharing takes place where the electrical current reaches the quench zone: the current follows a path through the copper stabilizer layer. Figure 9 shows this phenomenon, as simulated by the EFV method. Points in the middle of each layer are shown with different markers. The distance between points along the length of the tape is 0.005 m. After 0.03 s, the electric current has changed its path completely to the stabilizer and silver layers. The

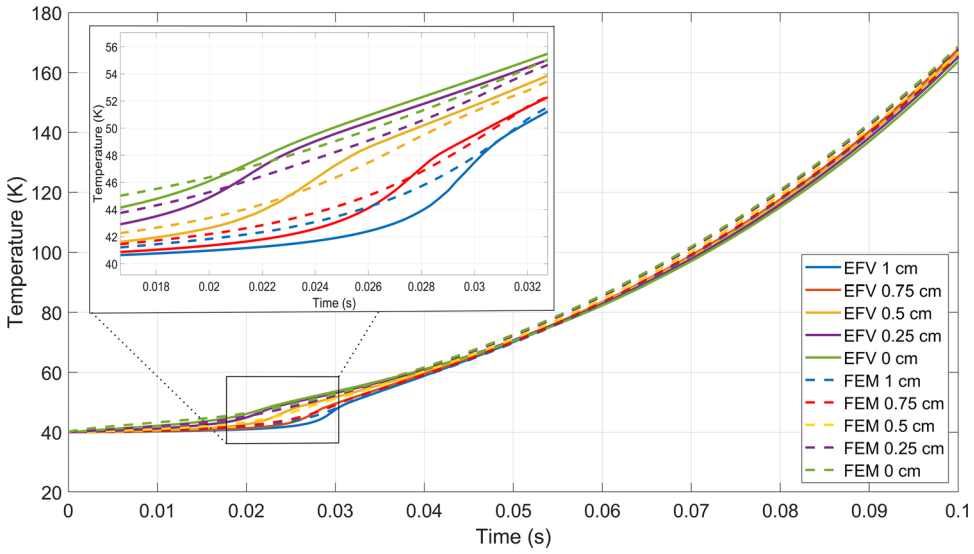

Fig. 7 Superconducting quench event: FEM versus EFV results for a 0.1 s simulation

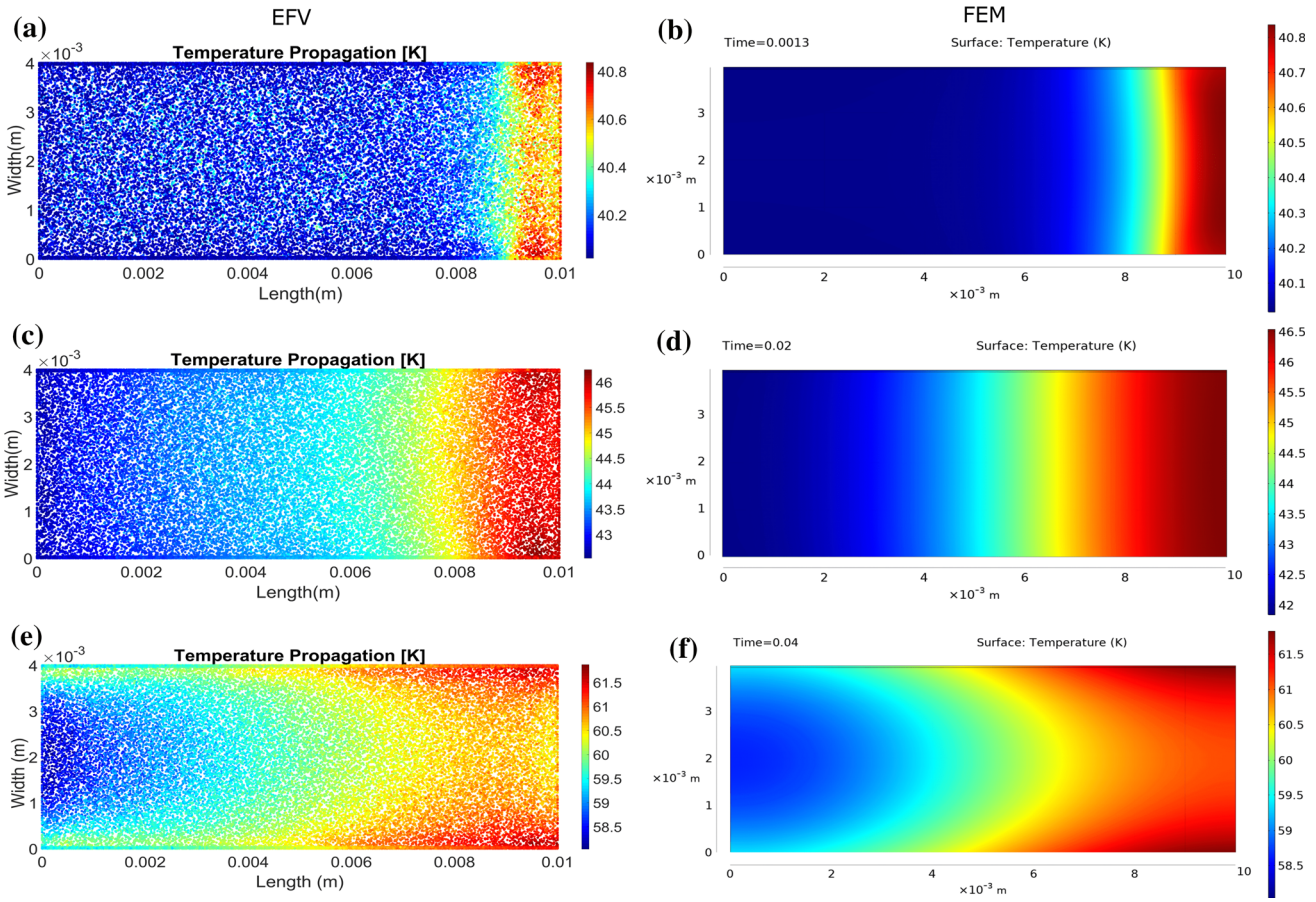

Fig. 8 Top view of temperature propagation on the YBCO tape in [K] at **a** EFV 0.0013 s, **b** FEM 0.0013 s, **c** EFV 0.02 s, **d** FEM 0.02 s, **e** EFV 0.04 s, **f** FEM 0.04 s

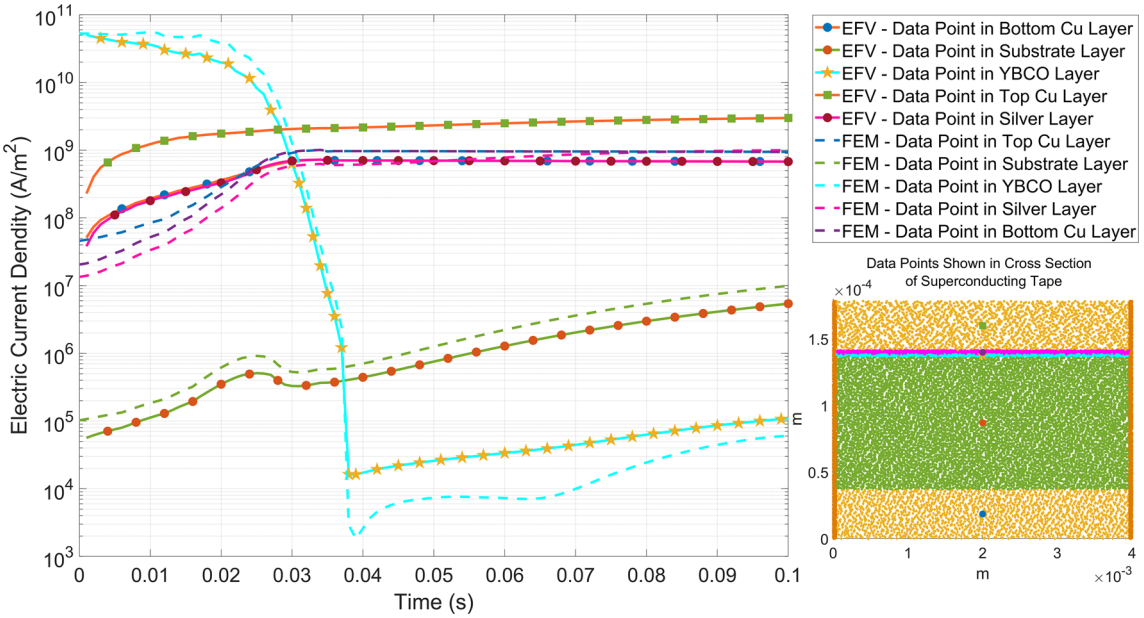

Fig. 9 Electric current sharing in the YBCO tape during the quench phenomenon

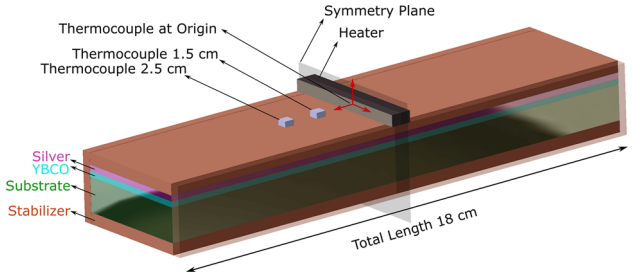

Fig. 10 Experimental set-up: quench propagation in a short YBCO tape, presented in [32]–[33]

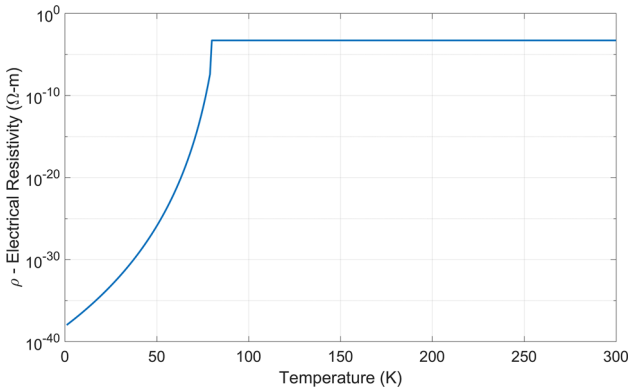

Fig. 11 Electrical resistivity of YBCO layer against temperature, for $n = 21$

dashed line represents current sharing in the simulation done using FEM.

3.2 Effective floating volume: predictions compared to experimental measurements

Besides the benchmark against state-of-the-art FEM software shown above, quench data presented in [32–34] was used to benchmark the capabilities of the proposed EFV method. A YBCO tape with the same geometry as shown in Fig. 5 has been experimentally and numerically studied for quench simulation. Figure 10 shows the experimental setup. Quench excitation was done using a heater at the center of a 9 cm long YBCO tape. Since quench propagation is symmetrical, only half the length of the tape was considered in the simulation. The thermocouples in the experiment were connected to the top stabilizer layer at distances of 0, 1.5 and 2.5 cm to the heater, to acquire the temperature profile (in time) during quench propagation. The heater half-length is 1.5 mm. The tape is initially at temperature $T_0 = 70$ K. The experiment was done with a ratio of current to critical current $I/I_{cr} = 0.5$, where the critical current is approximately $I_{cr} = 70$ A [33] (Fig. 8a). Equation (32) was used to estimate the electrical resistivity of the YBCO layer, with n = 21 and $E_c = 10^{-4}$ V/m In the previous section (comparing EFV and FEM) $n = 30$ was used; the difference takes into account the change in material properties of the superconducting tape in the transition region from superconducting to normal conducting state after critical temperature T_{cr}. Figure 11 shows the electrical resistivity of the YBCO layer for the given operational conditions and n value.

$$\rho\,(B,T,I) = \begin{cases} \frac{E_c}{I_c(B,T)} \cdot \left(\frac{I}{I_{cr}(B,T)}\right)^{n-1} & for \quad T < T_{cr} \\ 500\ \mu\Omega \cdot \mathrm{m} & for \quad T > T_{cr} \end{cases} \tag{32}$$

Total simulation time was set to 10 s to match the available experimental data. The sample time $\tau = 0.01$ s leads to 1000 time steps. The minimum energy that is required to initiate quench is called minimum quench energy. The minimum quench energy (MQE) is equal to 0.67 J for $I/I_{cr} = 0.5$ (in Table II [34]). The duration of the current pulse applied to the heater was set to 1 s. At each time step, the energy transferred to the first 1.5 mm of tape is $dMQE = \frac{MQE \cdot \tau}{duration\ of\ pulse}$. To calculate the temperature rise at the heater at each time step, the mean density and mean heat capacity of the portion of tape under the heater is calculated as:

$$\begin{aligned} \mathrm{P}_M &= \mathrm{P}_{Cu}\mathrm{V}_{f_{Cu}} + \mathrm{P}_{Ag}\mathrm{V}_{f_{Ag}} + \mathrm{P}_{subs}\mathrm{V}_{f_{subs}} \\ &\quad + \mathrm{P}_{YBCO}\mathrm{V}_{f_{YBCO}} \end{aligned} \tag{33}$$

$$\begin{aligned} \mathrm{C}_{p\_M} &= \mathrm{C}_{p\_Cu}\mathrm{V}_{f_{Cu}} + \mathrm{C}_{p\_Ag}\mathrm{V}_{f_{Ag}} + \mathrm{C}_{p\_subs}\mathrm{V}_{f_{subs}} \\ &\quad + \mathrm{C}_{p\_YBCO}\mathrm{V}_{f_{YBCO}} \end{aligned} \tag{34}$$

where is the mass density (kg/m^3) and V_f is the volume fraction. The specific heat capacity C_p is updated as function of temperature. The temperature rise due to the heater was propagated using Eq. (22) and then stored. Since temperature was measured at the thermocouple locations (T_0, $T_{1.5}$ and $T_{2.5}$), the EFV solution was extracted at these location during the 10 s simulation. Results from the FEM solution (provided in [32]) are also included in Fig. 12. Both numerical simulations have larger magnitudes and steeper slopes compared to the measurements. This could be due to inaccuracy on material properties, convective cooling introduced by the environment in the measurements, or interfacial thermal resistance between layers of the superconductor tape. In conclusion, the trend and overall results of the EFV simulation as compared to both the FEM simulation and the published experimental results illustrate the validity of the proposed EFV method.

4 Computational performance

One of the most important motivations for the development of the EFV algorithm is to achieve a significant reduction in simulation time compared to conventional numerical methods such as FEM. The parallelization of the EFV algorithm

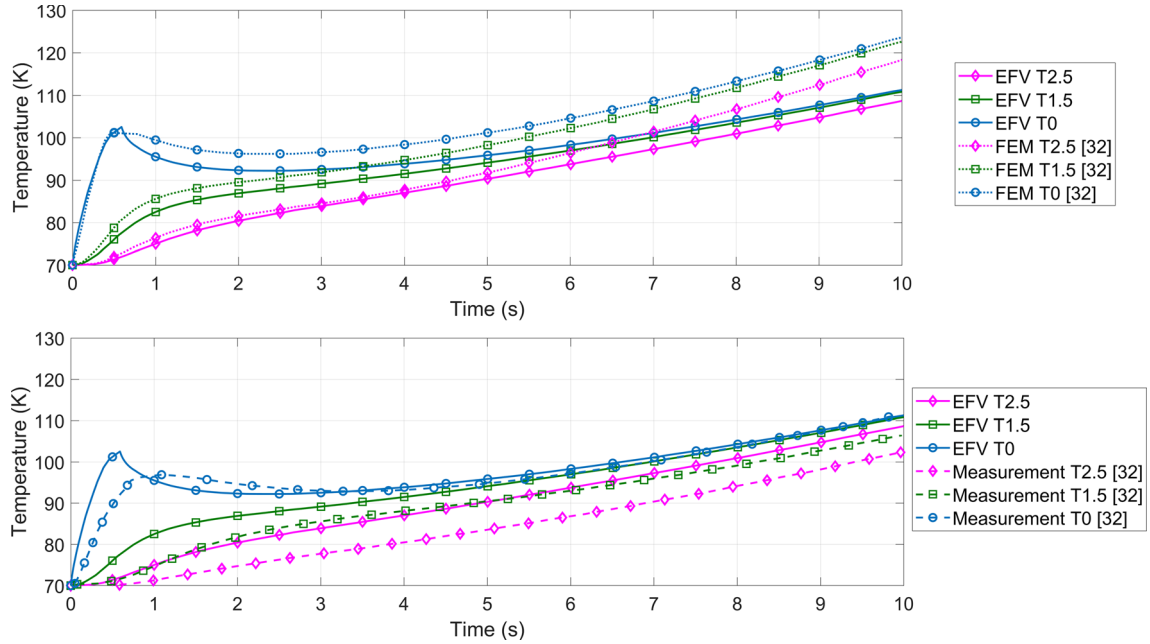

Fig. 12 Temperature profile at locations T_0, $T_{1.5}$, $T_{2.5}$. Comparison of EFV, FEM and measurements [32]

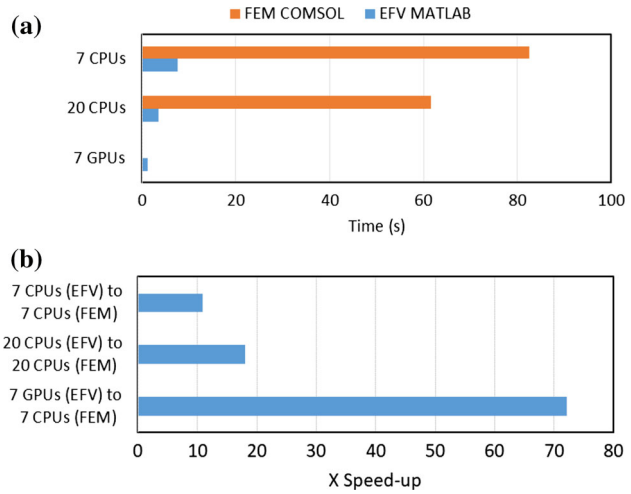

Fig. 13 **a** Performance of EFV against FEM. Shorter simulation time indicates better performance. **b** Speed ratios

is based on the Monte-Carlo method: the time history of each particle can be programmed into a single GPU core in a GPU engine since the solution for each particle is independent of each other. In this section, a comparison of the simulation time of EFV versus FEM (for the example shown in Sect. 3.1) is presented. The workstation used for this study has 20 CPU cores (dual 10-core Intel Xeon E5-2697v3 CPUs) and seven Titan V NVidia GPUs, with a total of 35,840 CUDA cores. Figure 13a shows simulation time on CPU–CPU comparison, with both methods using the same number of CPUs in parallel. Figure 13b shows speed ratios (FEM time/EFV time). Speed increases of 18× and 11× are achieved using the EFV method compared to FEM for 20 and 7 CPUs in parallel, respectively. The simulation time for each FEM iteration is approximately 61.53 s (when using 20 CPU cores) and 82.61 s (using 7 CPU cores), while the corresponding values for EFV are 3.42 and 7.571 s, respectively. The number of nodes used in FEM is equal to the number of particles used in the EFV method (approximately 40,000). EFV was implemented as a single program, multiple data (SPMD) code in MATLAB, using the GPU support toolbox. A GPU–GPU comparison could not be accomplished since the FEM software used does not support GPU computing. A baseline comparison was performed by running the FEM model in 7 CPU cores, while the SPMD MATLAB code ran the EFV method on 7 GPUs; each GPU handling approximately 5700 points of the solution domain. After each iteration, the GPUs broadcast the simulation results to the other GPUs to update material properties. Using 7 CPU cores in parallel, each FEM iteration took 82.61 s, while one iteration using the EFV method on 7 GPUs took 1.145 s. This represents in excess of 72× speed up in simulation time. For prototype purposes, MATLAB was used to implement the method in both CPU and GPU platforms—implementing EFV on lower-level programming languages (such as CUDA/C++) would lead to significantly better performance. In a conventional computer (no GPU), the speed-up improvement by the EFV method is much better than FEM as the number of CPU cores increases (Fig. 12a). The performance comparison is done based on average time elapsed at one iteration. The time required to mesh in FEM and to perform the EFV and find probable acquisition points are not included as this pro-

cess is done only once before beginning of time sequence of simulation. For the purpose of comparing computational performance, the FEM simulation was set to have the same number of iterations and time step as the EFV.

5 Conclusions

The effective floating volume method (EFV) is presented as a novel approach to solve multiphysics problems in multi-scale systems that eliminates the numerical bottleneck in conventional FEM tools: the need to invert a large matrix at each time step of a transient simulation. With currently available FEM software tools, the number of elements needed to achieve reasonable accuracy in multi-scale problems can make simulation time prohibitively long. A demonstration example using joule heating combined with heat conduction and electrical current sharing has been presented. The proposed formulation takes into account the temperature, voltage and temperature-dependent material properties at the acquisition points, not only at the boundaries but also along the radial path of energy transfer. Therefore, the proposed EFV method can either eliminate or drastically reduce the need for scattered interpolation, compared to previous mesh-free methods. These features enable the proposed method to tackle problems with multi-scale geometries, such as the simulation of composite objects with thin layers. The proposed method is well suited for GPU parallelization (one computation thread per GPU core), as made available by state-of-the-art GPU computers. This enables the simulation of complex multiphysics multi-scale problems, where conventional FEM software tools would require large numbers of elements, leading to prohibitively long simulation times. It is shown that EFV converges to correct results, as compared to both FEM simulations and available experimental measurements, while its simulation time is a fraction of the one needed when using FEM. The proposed method points a path of future development to extend the proposed concept to other physical domains, including stress-strain, thermal-stress, heat transfer in porous media, fluid mechanics, and electromagnetics.

Acknowledgements This work has been partly supported by the National Science Foundation, PFI Award 1827730, 2018.

References

1. Hermet J, Bottin F, Dezanneau G, Geneste G (2013) Kinetic Monte Carlo study of protonic diffusion and conduction in Gd-doped BaCeO3. Solid State Ion 252:48–55
2. Li Q, Ye W (2017) An interfering Monte Carlo method for partially coherent phonon transport in superlattices. Int J Heat Mass Transf 107:534–543
3. Tang DS, Cao BY (2017) Ballistic thermal wave propagation along nanowires modeled using phonon Monte Carlo simulations. Appl Therm Eng 117:609–616
4. Shomali Z, Pedar B, Ghazanfarian J, Abbassi A (2017) Monte-Carlo parallel simulation of phonon transport for 3D silicon nano-devices. Int J Therm Sci 114:139–154
5. Pan C, Chávez O, Romero CE, Levy EK, Corona AA, Rubio-Maya C (2016) Heat mining assessment for geothermal reservoirs in mexico using supercritical CO_2 injection. Energy 102:148–160
6. Xu J, Zhang W, Sun R (2016) Efficient reliability assessment of structural dynamic systems with unequal weighted quasi-Monte Carlo simulation. Comput Struct 175:37–51
7. Hua YC, Cao BY (2017) Cross-plane heat conduction in nanoporous silicon thin films by phonon Boltzmann transport equation and Monte Carlo simulations. Appl Therm Eng 111:1401–1408
8. Deng ZS, Liu J (2002) Monte Carlo method to solve multidimensional bioheat transfer problem. Numer Heat Transf B Fundam 42(6):543–567
9. Netter D, Leveque J, Masson P, Rezzoug A (2004) Monte Carlo method for transient eddy-current calculations. IEEE Trans Magn 40(6):3450–3456
10. Fraley SK, Hoffman T, Stevens P (1980) A Monte Carlo method of solving heat conduction problems. J Heat Transf 102(1):121–125
11. Karl S (2019) First passage Monte Carlo algorithms for solving coupled systems of diffusion–reaction equations. Appl Math Lett 88:141–148
12. Hurtado J, Barbat AH (1998) Monte Carlo techniques in computational stochastic mechanics. Arch Comput Methods Eng 5(1):3
13. Hardin TJ (2019) Accelerating coupled finite element-kinetic Monte Carlo models: 200 × speedup of shear transformation zone dynamics simulations. Comput Mech 63(3):511–520
14. Pisaroni M, Nobile F, Leyland P (2017) A continuation multi level Monte Carlo (C-MLMC) method for uncertainty quantification in compressible inviscid aerodynamics. Comput Methods Appl Mech Eng 326:20–50
15. Shentu J, Yun S-H, Cho NZ (2007) A Monte Carlo method for solving heat conduction problems with complicated geometry. Nucl Eng Technol 39(3):207–214
16. Cho BH, Cho NZ (2010) Monte Carlo method extended to heat transfer problems with non-constant temperature and convection boundary conditions. Nucl Eng Technol 42(1):65–72
17. Rosca VE, Leitão VM (2008) Quasi-Monte Carlo mesh-free integration for meshless weak formulations. Eng Anal Bound Elem 32(6):471–479
18. Gong F, Papavassiliou DV, Duong HM (2014) Off-lattice Monte Carlo simulation of heat transfer through carbon nanotube multiphase systems taking into account thermal boundary resistances. Numer Heat Transf A Appl 65(11):1023–1043
19. Gupta A, Arun C (2018) Stochastic meshfree method for elastic buckling analysis of columns. Comput Struct 194:32–47
20. Haji-Sheikh A, Sparrow E (1966) The floating random walk and its application to Monte Carlo solutions of heat equations. SIAM J Appl Math 14(2):370–389
21. Bahadori R, Gutierrez H, Manikonda S, Meinke R (2017a) Monte Carlo method simulation for two-dimensional heat transfer in homogenous medium and proposed application to quench propagation simulation. IEEE Trans Appl Supercond 27(4):1–5
22. Bahadori R, Gutierrez H, Manikonda S, Meinke R (2017b) Two-dimensional transient heat conduction in multi-layered composite media with temperature dependent thermal diffusivity using floating random walk Monte-Carlo method. Int J Heat Mass Transf 115:570–580
23. Bahadori R, Gutierrez H, Manikonda S, Meinke R (2018) A mesh-free Monte-Carlo method for simulation of three-dimensional transient heat conduction in a composite layered material with

temperature dependent thermal properties. Int J Heat Mass Transf 119:533–541
24. Gingold RA, Monaghan JJ (1977) Smoothed particle hydrodynamics: theory and application to non-spherical stars. Mon Not R Astron Soc 181(3):375–389
25. Cleary PW, Monaghan JJ (1999) Conduction modelling using smoothed particle hydrodynamics. J Comput Phys 148(1):227–264
26. Shepard D (1968) A two-dimensional interpolation function for irregularly-spaced data. In: Proceedings of the 1968 23rd ACM national conference, ACM, pp 517–524
27. Onate E, Idelsohn S, Zienkiewicz O, Taylor R (1996) A finite point method in computational mechanics. applications to convective transport and fluid flow. Int J Numer Meth Eng 39(22):3839–3866
28. Chen W (2000) Boundary knot method: a meshless, exponential convergence, integration-free, and boundary-only RBF technique. arXiv:math/0004182
29. Zerroukat M, Power H, Chen C (1998) A numerical method for heat transfer problems using collocation and radial basis functions. Int J Numer Meth Eng 42(7):1263–1278
30. Haji-Sheikh A (1965) Application of Monte Carlo methods to thermal conduction problems. University of Minnesota
31. Minkowycz W, Sparrow E, Murthy J, Abraham J (2009) Handbook of numerical heat transfer, 2nd edn. Wiley, Hoboken. https://doi.org/10.1002/9780470172599
32. Chan WK, Masson PJ, Luongo C, Schwartz J (2010) Three-dimensional micrometer-scale modeling of quenching in high-aspect-ratio $YBa_2Cu_3O_{7-\delta}$ coated conductor tapespart i: model development and validation. IEEE Trans Appl Supercond 20(6):2370
33. Wang X, Trociewitz U, Schwartz J (2007) Near-adiabatic quench experiments on short $YBa_2Cu_3O_{7-\delta}$ coated conductors. J Appl Phys 101(5):053,904
34. Chan WK, Schwartz J (2011) Three-dimensional micrometer-scale modeling of quenching in high-aspect-ratio $YBa_2Cu_3O_{7-\delta}$ coated conductor tapespart ii: Influence of geometric and material properties and implications for conductor engineering and magnet design. IEEE Trans Appl Supercond 21(6):3628–3634